

Distribution of Inhomogeneities in the Interstellar Plasma in the Directions of Three Distant Pulsars from Observations with the RadioAstron Ground–Space Interferometer

M. V. Popov^{1*}, A. S. Andrianov^{1**}, N. Bartel^{2***}, C. Gwinn^{3****}, B. C. Joshi^{4*****},
D. Jauncey^{5*****}, N. S. Kardashev^{1*****}, A. G. Rudnitskii^{1*****}, T. V. Smirnova^{6,1*****},
V. A. Soglasnov^{1*****}, E. N. Fadeev^{1*****}, and V. I. Shishov^{6,1*****}

¹*Astro Space Center, P.N. Lebedev Physical Institute, Russian Academy of Sciences,
Profsoyuznaya ul. 84/32, Moscow, 117997 Russia*

²*Department of Physics and Astrophysics, York University, Toronto, Canada*

³*Department of Physics, University of California Santa Barbara, Santa Barbara, California, USA*

⁴*National Center for Radio Astrophysics, Pune, India*

⁵*CSIRO Astronomy and Space Science, and Research School of Astronomy and Astrophysics,
Australian National University, Canberra, Australia*

⁶*Pushchino Radio Astronomy Observatory, Astro Space Center, P.N. Lebedev Physical Institute,
Russian Academy of Sciences, Pushchino, Moscow region, Russia*

Received December 29, 2015; in final form, February 17, 2016

Abstract—The RadioAstron ground–space interferometer has been used to measure the angular sizes of the scattering disks of the three distant pulsars B1641–45, B1749–28, and B1933+16. The observations were carried out with the participation of the Westerbork Synthesis Radio Telescope; two 32-m telescopes at Torun, Poland and Svetloe, Russia (the latter being one antenna of the KVAZAR network); the Saint Croix VLBA antenna; the Arecibo radio telescope; the Parkes, Narrabri (ATCA), Mopra, Hobart, and Ceduna Australian radio telescopes; and the Hartebeesthoek radio telescope in South Africa. The full widths at half maximum of the scattering disks were 27 mas at 1668 MHz for B1641–45, 0.5 mas at 1668 MHz for B1749–28, and 12.3 at 316 MHz and 0.84 mas at 1668 MHz for B1933+16. The characteristic time scales for scatter-broadening of the pulses on inhomogeneities in the interstellar plasma τ_{sc} were also measured for these pulsars using various methods. Joint knowledge of the size of the scattering disk and the scatter-broadening time scale enables estimation of the distance to the effective scattering screen d . For B1641–45, $d = 3.0$ kpc for a distance to the pulsar $D = 4.9$ kpc, and for B1749–28, $d = 0.95$ kpc for $D = 1.3$ kpc. Observations of B1933+16 were carried out simultaneously at 316 and 1668 MHz. The positions of the screen derived using the measurements at the two frequencies agree: $d_1 = 2.6$ and $d_2 = 2.7$ kpc, for a distance to the pulsar of 3.7 kpc. Two screens were detected for this pulsar from an analysis of parabolic arcs in the secondary dynamic spectrum at 1668 MHz, at 1.3 and 3.1 kpc. The scattering screens for two of the pulsars are identified with real physical objects located along the lines of sight toward the pulsars: G339.1–04 (B1641–45) and G0.55–0.85 (B1749–28).

DOI: 10.1134/S1063772916090067

*E-mail: popov069@asc.rssi.ru

**E-mail: andrianov@asc.rssi.ru

***E-mail: bartel@yorku.ca

****E-mail: cgwinn@physics.ucsb.edu

*****E-mail: bcj@ncra.tifr.res.in

*****E-mail: David.Jauncey@csiro.au

*****E-mail: nkardash@asc.rssi.ru

*****E-mail: arud@asc.rssi.ru

*****E-mail: tania@prao.ru

*****E-mail: vsoglasn@asc.rssi.ru

*****E-mail: fadeev@asc.rssi.ru

1. INTRODUCTION

The radio emission of astronomical objects is scattered on inhomogeneities in the interstellar plasma. The effects of this scattering are most clearly manifest for compact sources, such as pulsars. It was precisely with the discovery of pulsars that the scattering of radio waves on inhomogeneities in the interstellar plasma was first studied theoretically [1–3]

*****E-mail: shishov@prao.ru

and observationally [4–6]. The main consequences of this scattering are the following behavior angular broadening of the source θ_{sc} , increase in the pulse duration τ_{sc} , and modulation of the radio intensity with frequency and time, on the characteristic scales $\Delta\nu_d$ and Δt_{sc} .

Simultaneous measurements of the above parameters for a given object during a sufficiently long time interval ($T > \Delta t_{sc}$) and over a sufficiently broad frequency band ($B_\nu > \Delta\nu_d$) can be used to obtain information about the structure of the inhomogeneities in the interstellar plasma in the direction of this object. Very Long Baseline Interferometry (VLBI) observations are advantageous for studies of scattering effects, since only in such observations is it possible to directly measure the scattering angle θ_{sc} [7, 8]. New possibilities for VLBI observations are provided by the RadioAstron ground–space interferometer, which can realize high angular resolutions of up to 1 milliarcsecond (mas) at meter wavelengths (92 cm) and up to 0.2 mas at decimeter wavelengths (18 cm). The diameters of the scattering disks of the pulsar B0329+54 (4.7 mas) [9] and the Crab pulsar (14.0 mas) [10] have been measured at 316 MHz. The distance to scattering and refractive layers of the interstellar medium have been determined for the nearby pulsar B0950+08 [11]. Here, we present measurements of scattering effects for the pulsars B1641–45 and B1749–28 at 18 cm, and for the pulsar B1933+16 at 18 cm and 92 cm.

2. OBSERVATIONS AND REDUCTION

Table 1 presents information about the observing sessions. Fairly long observing sessions were organized, intended to provide sufficient statistical material for reliable determination of scattering parameters such as the characteristic scintillation time scale Δt_{sc} and the decorrelation bandwidth $\Delta\nu_d$. It was also important to trace the variations of the visibility-function amplitudes as functions of the projected baselines. Due to the conditions for the thermal regime of the onboard data-transmission system, the duration of a continuous scientific session with the spacecraft cannot exceed a specified time, one to two hours, depending on the orientation of the spacecraft relative to the Sun. Therefore, the time interval covered by observations with the space radio telescope (SRT) is indicated separately in the column “Time with SRT”. The SRT data were subject to one-bit digitization, and the data obtained at the ground telescopes to two-bit digitization.

Another important aspect of the 92 cm observations is that only the upper frequency sideband (316–332 MHz) provides useful information, due to the characteristics of the input filter of the receiver system. At other frequencies, both the upper and lower

sidebands are recorded, each with a width of 16 MHz, for two circular polarizations. Table 1 gives the central frequency (i.e., the frequency dividing the bands). The SRT is also able to operate simultaneously at two frequencies, with the different frequency channels receiving the radio signal in different polarizations. This was the regime used for the observations of B1933+16. The actual characteristics of the onboard radio-astronomy complex are given in [12].

The data were correlated on the correlator of the Astro Space Center (ASC) of the P.N. Lebedev Physical Institute, using a pulse window and compensating for the smearing of the pulse due to dispersion. The main characteristics of this correlation method are described in [13]. Table 2 presents the main parameters adopted during the correlation: the number of channels N_{ch} and readout interval of the correlator δt , which must be a multiple of the pulsar period. The integration time for each pulse was chosen to equal the pulse width at 10% of the maximum intensity (on-pulse). The second integration window was chosen to have the same duration outside the main pulse (off-pulse). This window was used to compute normalization coefficients using formulas (1) and (2) (see Section 3). All necessary information about the pulsars, including the ephemerides of the pulse arrivals, were taken from the ATNF pulsar catalog [14].¹ The phase of the pulse maximum was determined via a preliminary computation on the correlator by analyzing the auto-correlation spectrum for the largest ground-based radio telescope. Complex cross-correlation spectra for all baselines are formed at the correlator output, including auto-correlation spectra and cross-polarization spectra, in standard FITS format. The subsequent analysis of the correlated data was carried out using the standard package for reading FITS files CFITSIO [15].

3. GENERAL CONSIDERATIONS

It is usual to recognize three regimes for measurements of scintillation parameters [16]: a snapshot regime, when the analysis time is less than the characteristic time scale for diffractive scintillations Δt_{sc} and the receiver bandwidth is less than the decorrelation bandwidth $\Delta\nu_d$ for diffractive distortions in the spectrum; an averaging regime, when the analysis time is appreciably longer than Δt_{sc} and the receiver bandwidth is much wider than $\Delta\nu_d$; and finally, an ensemble-averaging regime, which involves averaging of many realizations obtained in an averaging regime over a time that exceeds the characteristic time scale for refractive scintillations Δt_{ref} . The time scales for diffractive scintillations lie in the range from

¹ <http://www.atnf.csiro.au/people/pulsar/psrcat/>

Table 1. Information on observing sessions

Pulsar	P , s	Dispersion measure, pc/cm ³	Frequency, MHz	Date	Total time, hours	Time with SRT, hours	Telescopes
B1641–45	0.455	478.8	1668	18.03.2014	15	1.0, 0.7, 2.0	At, Mp, Cd, Ho, Hh, Pa
B1749–28	0.562	50.37	1668	26.05.2014	6	0.7, 0.7, 1.0	At, Mp, Cd, Ho, Hh, Pa
B1933+16	0.359	158.52	1668/316	01.08.2013	1.5	1.5	Wb, Sc, Ar, Tr, Sv

Table 2. Main parameters used when correlating the pulsar cross-correlation spectra and the results obtained

Pulsar	N_{ch}	δt , s	ΔT , s	Δt_{sc} , s	$\Delta\nu_d$, kHz	τ_{sc} , μs	θ_{H} , mas	l , deg b , deg	D , kpc	d , kpc
B1641–45	16 384	0.45	115	0.20 (0.05)	0.062 (0.002)	2600 (100)	27 (5)	339.2, –0.2	4.9	3.0
B1749–28	256	5.62	225	220 (20)	410 (100)	0.310 (0.040)	0.5 (0.2)	1.54, –0.96	1.3	0.95
B1933+16	2048	0.35	250	41.6 (0.5)	50.4 (1.1)	3.2 (0.1)	0.84 (0.04)	52.4, –2.1	3.7	2.7 [1.3; 3.1]
B1933+16	8192	0.35	250	–	0.25 (0.15)	600 (400)	12.3 (0.6)	52.4, –2.1	3.7	2.6

N_{ch} is the number of correlator channels, δt the cross-correlation spectrum readout interval, ΔT the cross-spectrum analysis interval, Δt_{sc} the characteristic scintillation time scale, $\Delta\nu_d$ the decorrelation bandwidth, τ_{sc} the time scale for scatter broadening of the pulse due to inhomogeneities in the interstellar plasma, θ_{H} the angular diameter of the scattering disk, l and b the Galactic coordinates of the pulsar, D the distance to the pulsar, and d the distance to the scattering screen. The uncertainties (rms deviations) are given in parentheses. For B1933+16, the results obtained at 316 MHz are given in the first row (estimates of d obtained using the parabolic arcs are shown in square brackets), and those obtained at 1668 MHz in the second row.

seconds to tens of minutes, while the characteristic time scales for refractive scintillations are typically several weeks or months. Thus, we can apply only the snapshot or averaging regimes in our analysis. The snapshot regime provides the possibility of analyzing the behavior of instantaneous values of the visibility-function amplitude, and to identify structure in the scattering disk, while the averaging regime enables the acquisition of mean values of the scattering disk size θ_{H} and the scattering time scale τ_{sc} , which enables estimation of the position of the scattering screen along the line of sight.

The interferometer response for a given pair of telescopes, called the visibility function, is derived from the set of complex cross-correlation spectra via successive Fourier transformations, first in frequency (the inverse Fourier transform) and then in time (the direct transform), on a time interval ΔT . The visibility function is analyzed on a delay–fringe frequency diagram, $V_{\text{AB}}(\tau, f)$. The main relations and transformations for the functions used in the post-correlation analysis are given in [9].

A snapshot of the scattered image of a pulsar

consists of individual coherent copies of the initial unscattered image distributed within the scattering disk. The signals from the secondary images are the same, but they arrive at the observation point with different time delays. For the case of such two-element interferometer two characteristic scales appear in the correlation function in a natural way: one corresponds to the size of the scattering disk (long delays) and the other to the distance between point images (small delays). Moreover, various other scales can also appear if several local regions of interstellar plasma with different physical parameters are present along the line of sight.

For a point source such as a pulsar, that is subject to scattering, the modulus of the visibility function for a sufficiently long baseline that resolves the scattering disk is a spot of increased amplitude with dimensions $\Delta f = 1/(2\pi\Delta t_{\text{sc}})$ and $\Delta\tau = 1/(2\pi\Delta\nu_d)$ in the frequency–time diagram. Precisely this form was demonstrated by an analysis of observations of the pulsar B0329+54 on ground–space baselines reaching 235 000 km [9]. On shorter baselines, when both radio telescopes were located within a single

diffraction spot, the visibility function has a peak at the coordinate origin (when the frequency and the delay are correctly compensated); the amplitude of this peak decreases with increasing baseline, enabling measurement of the size of the scattering disk [9].

The radio emission of pulsars possesses characteristic properties that require a special approach to calibrating the visibility amplitude. These properties include strong variability of the radio flux and modulation of the intensity due to scintillation. In VLBI observations of pulsars, it is usual to switch off automatic control of the receiver gain in order to avoid having it be triggered by strong pulsar pulses. As a result, the traditional method of calibrating the amplitudes by calculating the contribution of the signal from a studied source to the total antenna temperature based on measurements of the system temperatures of the participating telescopes and knowledge of the total flux of the studied source is not suitable for pulsars. The impulsive character of the emission and comparatively high flux densities of individual pulses make it possible to directly measure relative growths of the signal in the correlation window. A simple calibration relation can then be used. The calibration factor on which the visibility amplitudes must be divided has the form

$$R = \sqrt{(\sigma_{1\text{TOT}}^2 - \sigma_{1\text{OFF}}^2)(\sigma_{2\text{TOT}}^2 - \sigma_{2\text{OFF}}^2)}, \quad (1)$$

where the subscripts “1” and “2” denote the two telescopes in a pair and “ σ_{TOT}^2 ” and “ σ_{OFF}^2 ” are formally calculated as the amplitudes of the visibility function obtained from the auto-correlation spectra for the pulse window (TOT) and for the window outside the pulse (OFF).

In view of the low sensitivity of the SRT compared to the ground radio telescopes, the difference $\sigma_{\text{TOT}}^2 - \sigma_{\text{OFF}}^2$ for the SRT is determined with low accuracy, and, in this case, we can use the expression

$$R = \frac{\sigma_{2\text{OFF}}}{\sigma_{1\text{OFF}}} (\sigma_{1\text{TOT}}^2 - \sigma_{1\text{OFF}}^2) \sqrt{\eta}, \quad (2)$$

where $\eta = SEFD_{\text{GRT}}/SEFD_{\text{SRT}}$ is the ratio of the equivalent system temperature for a ground radio telescope (GRT) and the SRT.

The behavior of the visibility function for a scintillating source was considered in detail by Gwinn et al. [4, 5] and Gwinn [17]. It turns out to be possible to use dimensionless estimates of the visibility amplitude for scintillating radio sources, ρ_{AB} , as a fraction of the total flux in the form of a ratio of the quantities measured by the correlator. The decrease in the visibility amplitude with increasing baseline length can serve as a measure of the ratio of the area beneath the

central peak and the area beneath the extended part in a cross section through the central peak in delay.

$$\rho_{\text{AB}}^2 = \frac{\int_{\Delta t} V(\tau, f_0) d\tau}{\int_{T-\Delta t} V(\tau, f_0) d\tau}, \quad (3)$$

where $\Delta t = 1/B$ and $B = 16$ MHz is the bandwidth.

In this section, the extended part (“spot”) can be represented by a Lorentzian function, $V(\tau) = Ab/\pi(\tau^2 + b^2)$, where b is the halfwidth of this function and the area beneath the curve is A . The use of the above ratio as a measure of the decrease in the visibility amplitude removes the need to calibrate the amplitude $V(\tau, f_0)$ itself.

4. THE PULSAR B1641–45

B1641–45 has a dispersion measure of 478.8 pc/cm³ and is located at a distance of 4–5 kpc [18] in the Galactic plane. This is the most distant pulsar investigated using the RadioAstron ground–space interferometer. The scattering time scale τ_{sc} listed in the ATNF catalog, which is 11.2 ms at 1 GHz, can be used to estimate the expected value at our frequency, 1668 MHz (in accordance with a fourth-order power law). This value is close to 1.5 ms, which corresponds to the estimated decorrelation bandwidth $\Delta\nu_{\text{d}} \approx 100$ Hz, based on the relation $2\pi\tau_{\text{sc}}\Delta\nu_{\text{d}} = 1$. Providing such a high frequency resolution in a 16 MHz band would require more than 160 000 channels at the ASC correlator, which was not foreseen in its design. Therefore, to estimate the real decorrelation bandwidth, we carried out auxiliary computations on computers of the Division of Space Radio Astronomy for a limited recording (20 minutes) with the Parkes Radio Telescope and the Australia Telescope Compact Array (ATCA, Narrabri). Coherent dispersion compensation [19, 20] was used, and the number of spectral channels was 524 288, which provided a frequency resolution of 30.517 Hz. Unfortunately, the performance of the computer was not sufficient to enable operation with this number of channels during the entire observing session for all baseline combinations.

Figure 1 presents a frequency cross section of the two-dimensional correlation function between the dynamic spectra obtained at Parkes and Narrabri (ATCA). The experimental points were fit with a Lorentzian function, and the decorrelation bandwidth has a halfwidth of 62 ± 2 Hz. The curve passing through the circles corresponds to a cross section shifted by one period. The observed tenfold decrease in the correlation coefficient can be used to estimate the scintillation time at the $1/e$ level to be 0.2 s. The number of channels specified in the ASC correlator was 16 384, with the correlator data read out during

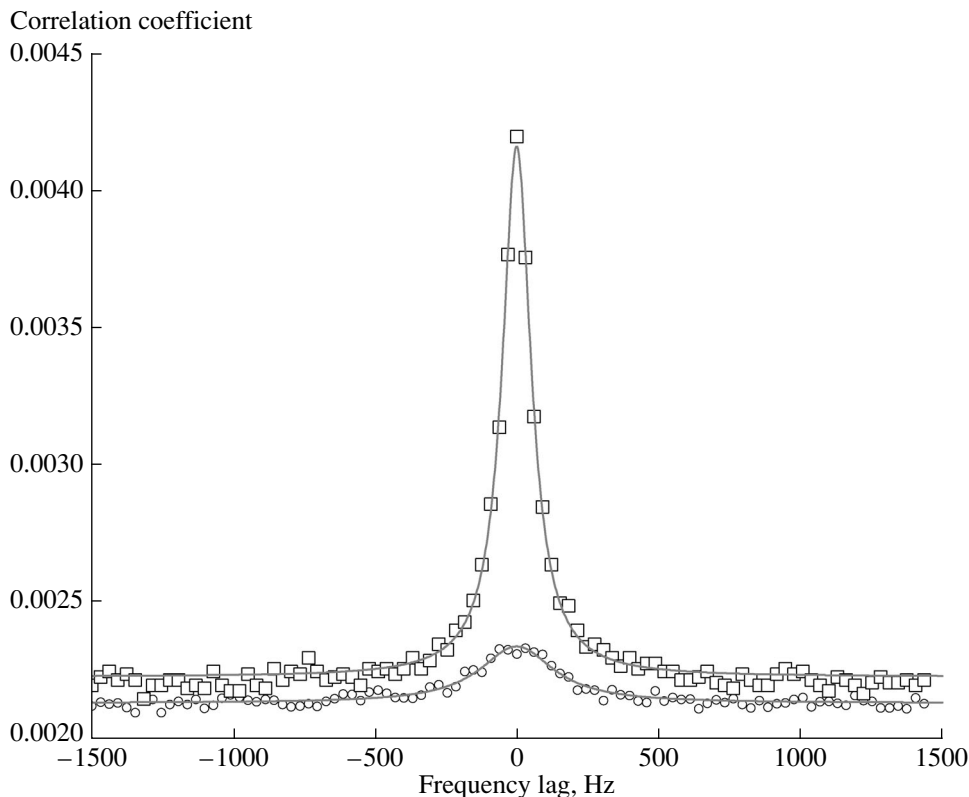


Fig. 1. The pulsar B1641–45. Frequency cross section of the two-dimensional correlation function between the dynamic spectra constructed for Parkes and Narrabri (ATCA) based on a 20 minute observing interval. The squares show data for a cross section with zero time shift, and the circles a cross section corresponding to a time shift of one pulsar period. The measured decorrelation bandwidth was 62 Hz.

each pulsar period with an integration window of 10 ms. The visibility amplitude was measured in each sequence of 256 pulses; i.e., at intervals of $\Delta T = 115$ s. Thus, our analysis was carried out in an averaging regime. For this pulsar, we used the direct method of calibrating the visibility amplitude using (1), since we considered only baselines involving ground radio telescopes with high sensitivities.

The calibrated visibility amplitudes for various baselines as a function of the projected baseline are presented in Fig. 2a; the projected baselines reach more than eight million wavelengths for the ATCA–Ceduna baseline. The Hobart radio telescope provided consistent data only at the very beginning and very end of the observing session, although formally it functioned during the entire observing period. Figure 2a shows an appreciable decrease in the visibility amplitude in the transition to long projected baselines. We estimated the diameter of the scattering disk using the following expression presented in [21]:

$$V_{AB} = V_0 \exp \left\{ -\frac{1}{2} \left[\frac{\pi}{(2 \ln 2)^{0.5}} \frac{b \theta_H}{\lambda} \right]^{\alpha-2} \right\}, \quad (4)$$

where the parameter α corresponds to the index for the power-law spectrum of the plasma inhomogeneities (which we took to be four), b is the projected baseline, λ the wavelength, and θ_H the desired full width at half maximum (FWHM), which was 27 ± 5 mas, according to a fit of this function using Eq. (4), shown in Fig. 2a by the solid curve.

The total duration of the observing session for this pulsar was about 15 hrs. This provided good coverage of the UV plane, making it possible to image the scattering disk using conventional ground based VLBI methods. The relative sensitivities of the telescopes were estimated from the growth in the signal level of the pulsar, and the sensitivity curve (system equivalent flux density, SEFD) for each telescope was represented by a time-dependent polynomial function. On average, the SEFDs were 50, 100, 300, 750, and 2000 Jy for the Parkes, the ATCA, Mopra, Hobart, and Ceduna, respectively. The Astro Space Locator (ASL) program package was used to image the scattering disk using a classical CLEAN deconvolution and self-calibration to reconstruct the radio image of the pulsar [22]. The size of the map was 50 mas \times 50 mas. Figure 3 shows the UV coverage (right) and resulting image of the scattering

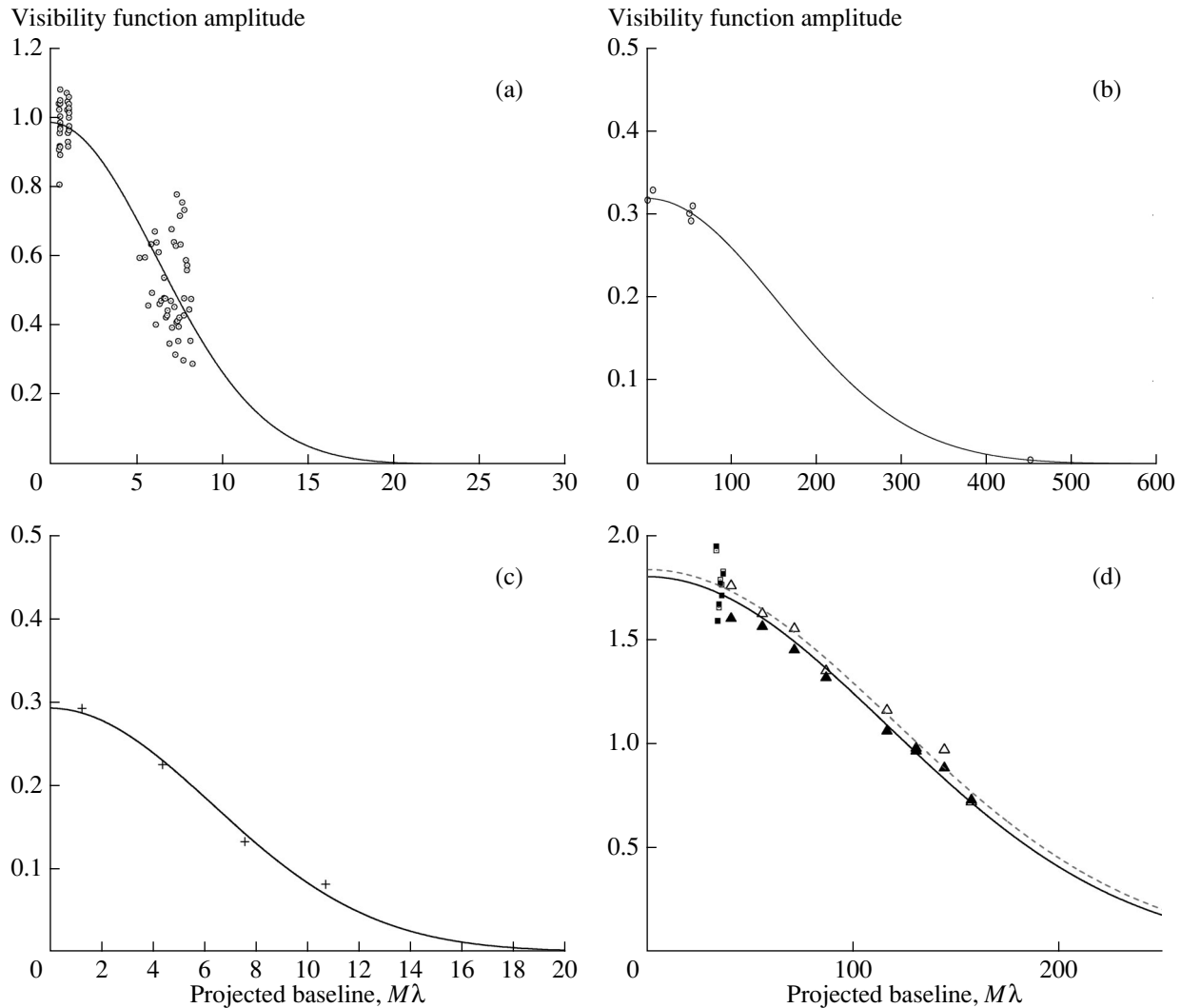


Fig. 2. Dependence of the visibility amplitude on the projected baseline for (a) B1641–45, where the solid curve corresponds to a scattering-disk diameter of 27 mas and only ground baselines were used; (b) B1749–28, calculated using (3), where the solid curve corresponds to a scattering-disk diameter of 0.5 mas; and for B1933+16 (c) at 316 MHz on the Westerbork–RadioAstron baseline and (d) at 1668 MHz on the Arecibo–RadioAstron (triangles) and Arecibo–Svetloe (pluses) baselines. The filled triangles and solid curves correspond to the upper sideband, and the hollow triangles and dashed curves to the lower sideband. The units of the X axis are millions of wavelengths.

disk (left), which appreciably exceeds the size of the synthesized beam of the interferometer. Fitting of the scattering disk with a two-dimensional Gaussian yields FWHM of $20.6 \text{ mas} \times 27.5 \text{ mas}$ in right ascension (RA) and declination (DEC), which agrees well with fitting of the dependence of the visibility amplitude on the projected baseline.

No signs of “spots” of enhanced visibility amplitude in the delay–fringe frequency diagram were found for this pulsar on ground–space baselines, and even on the intercontinental baselines between Australia and South Africa. This is not surprising, since the size of such a spot in delay should correspond to the characteristic scattering time scale, which we es-

timated above to be about 1.5 ms, while the correlator window was 1.024 ms.

To more accurately determine the scattering time scale τ_{sc} , we analyzed the shape of the mean pulse profile, which was obtained by applying a coherent dispersion compensation using a 20-minute recording of the signal received at the Parkes radio telescope. This was carried out in parallel with the construction of a dynamic spectrum with high spectral resolution, as was described at the beginning of this section. It turned out that the “tail” of the profile beyond the 10% intensity level could be fit well with an exponential function with a time constant of 2.6 ms. We identified this quantity with τ_{sc} . This estimate can be verified using the relation $2\pi\tau_{\text{sc}}\Delta\nu_{\text{d}} = 1$, since we

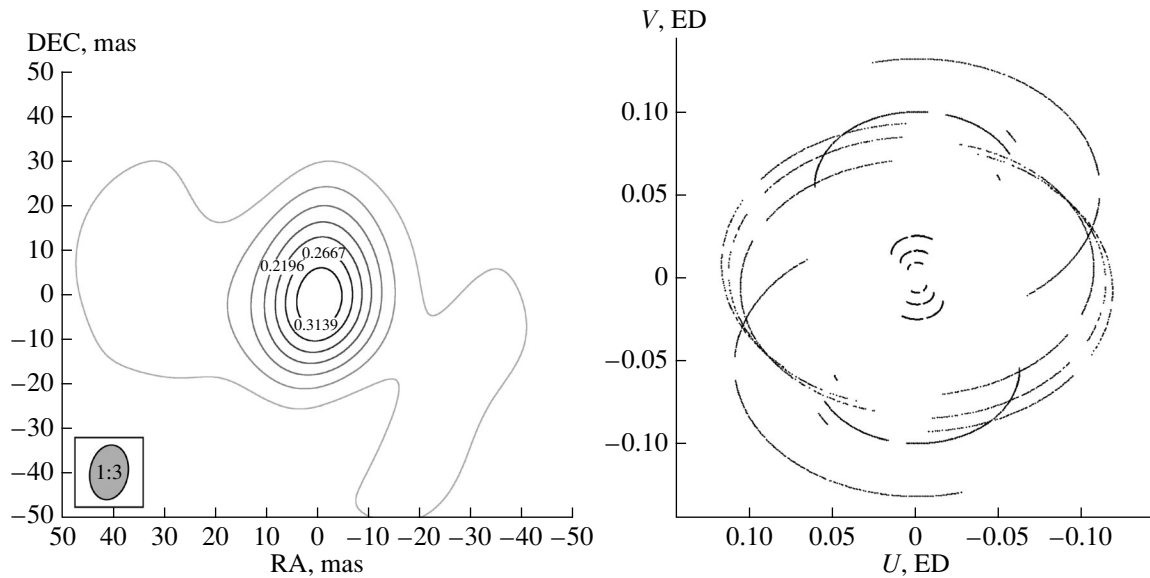


Fig. 3. Image of the scattering disk of B1641–45 obtained from the data for the ground radio telescopes. The UV coverage is shown on the right (coordinates of the baseline components U and V are given in Earth diameters), and the synthesized image is shown on the left. The RA and DEC are given in mas, and the size of the synthesized beam on a scale of 1:3 is shown in the lower left corner of the left panel.

have independently measured $\Delta\nu_d$. For the values of τ_{sc} and $\Delta\nu_d$ in Table 2, the above relation gives 1.01, confirming the consistency of our estimates of these scattering parameters.

Having at our disposal independent estimates of τ_{sc} and θ_H , we can make some conclusions about the distribution of the scattering medium along the line of sight between the observer and pulsar. We used the results of the analysis and revision of all distance measurements for the pulsar carried out by Verbiest et al. [18], which yield a range of possible distances from 4.1 to 4.9 kpc. Britton et al. [23] derived the relation for a uniform distribution of scattering plasma $\theta_H^2 = 16 \ln 2(c\tau_{sc}/D)$, which can be used to obtain the expected scattering angle for this case θ_H , where D denotes the distance to the pulsar. We obtained $\theta_H = 48\text{--}52$ mas, nearly twice the measured value. Thus, the hypothesis that the scattering medium is uniformly distributed along the line of sight is not consistent with our results.

Let us now turn to a model for the effective scattering screen. Britton et al. [23] also give a relation for this case:

$$\theta_H^2 = 8 \ln 2 c \tau_{sc} \left(\frac{D-d}{Dd} \right), \quad (5)$$

where D is the distance to the pulsar and d is the distance from the observer to the effective screen.

Our estimates for d were 2.7 kpc for a distance to the pulsar of 4.1 kpc (lower limit), and 3.0 kpc for a distance to the pulsar of 4.9 kpc (upper limit).

Two H II (ionized-hydrogen) regions lie in the direction toward B1641–45: G339.1–0.2 and G339.1–0.4 (the notation here corresponds to their Galactic coordinates). Weisberg et al. [24] present estimates of the distances to these two regions based on the radial velocities of radio recombination lines, which place G339.1–0.2 at a distance of 6.7 kpc and G339.1–0.4 at a distance of 3.3 kpc; i.e., the former is more distant than the pulsar while the latter is closer. Further, the location of G339.1–0.4 agrees to within 10% with our estimate of the distance to the effective scattering screen. Thus, this also refines the distance to the pulsar, which should be closer to 4.9 kpc.

5. THE PULSAR B1749–28

For this pulsar, we can select optimal values for the spectral and temporal resolutions of the correlator output data; it even proved possible to average the cross-correlation spectrum at the correlator over ten pulsar periods. To construct the dynamic spectrum presented in Fig. 4, we carried out additional averaging over four successive spectra, so that the time resolution became 22.5 s. The dynamic spectrum can be used to determine the characteristic decorrelation bandwidth $\Delta\nu_d$ and characteristic scintillation time scale Δt_{sc} . We determined these values by analyzing the central cross sections of the two-dimensional correlation functions between the dynamic spectra obtained in channels with left and right circular polarization. The frequency cross section could not be fit well using either a Lorentzian function or a

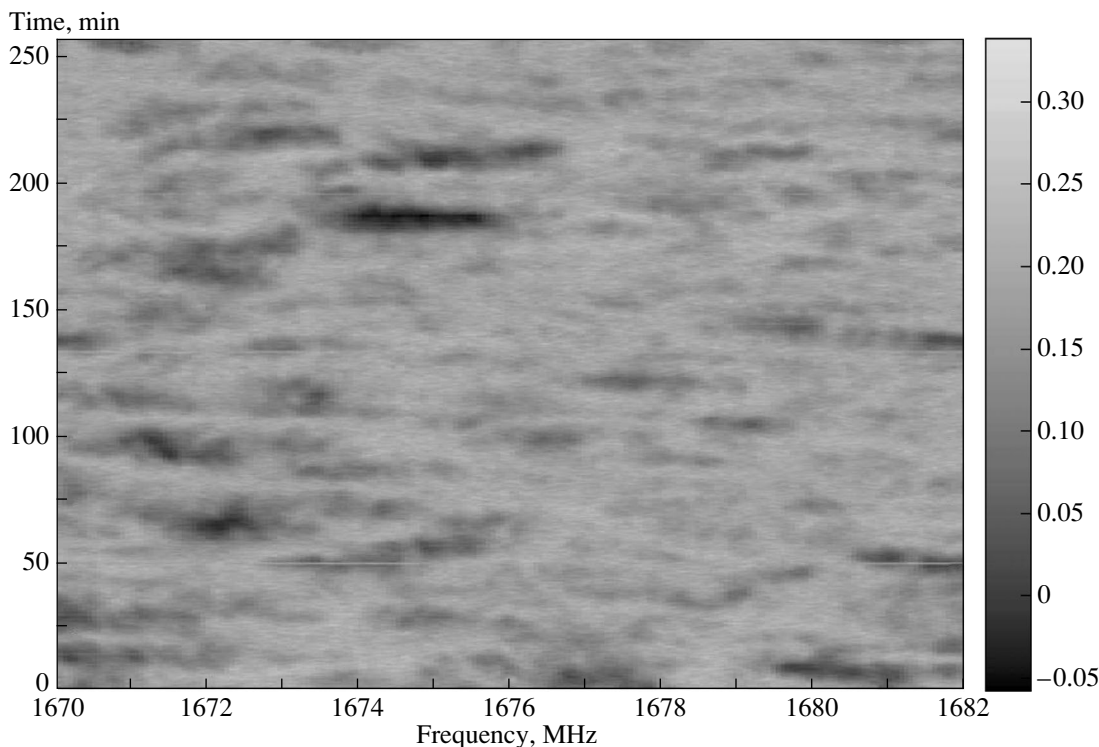


Fig. 4. Dynamic spectrum of B1749–28 constructed for a four-hour interval of observations with the Parkes radio telescope. The frequency resolution is 62.5 kHz, and the time step is 22.5 s. The measured decorrelation bandwidth is 410 kHz and the characteristic scintillation time scale is 220 s.

Gaussian. A fit with two Gaussians gave excellent agreement with the measured points. With this fit, $\Delta\nu_{1d} = 18$ kHz and $\Delta\nu_{2d} = 610$ kHz, with the amplitude (contribution) of the second component being twice that of the first.

We adopted a decorrelation bandwidth of 410 kHz for our subsequent analysis, which corresponds to the effective joint action of the fitted functions. The time cross section is fitted well by a Gaussian with a half width at the $1/e$ level of 220 ± 20 s. The visibility amplitude was determined in an interval of 225 s, which corresponds to a set of 40 cross-correlation spectra.

Thus, this essentially realized a snapshot regime, since the analysis time was roughly equal to the characteristic scintillation time scale $\Delta T \approx \Delta t_{sc}$. Accordingly, the visibility amplitude displays strong variations with time, with a modulation depth close to unity (Fig. 5). In this regime, calibration of the visibility amplitudes using (1) does not fully remove the observed scintillation, and an appreciable scatter in the calibrated values from 0.8 to 1.2 remains.

We then turned to an analysis of the structure of the visibility function as a function of the delay, in order to obtain the ratio of the compact an extended components, as described in Section 3. Figures 6a

and 6b show examples of cross sections of the interferometer response in the delay–fringe frequency diagram for two baselines: (a) Ceduna–Parkes and (b) RadioAstron–Parkes. The dashed curves show Lorentz functions that fit the observational data fairly well. On the ground–ground baseline, there is a compact feature in addition to the extended component, whose duration is determined by the width of the spectrum. This compact feature is not present on the ground–space baseline, indicating that the scattering disk was resolved on this baseline.

The ratio of the areas beneath the compact and extended components can serve as a measure of the visibility amplitude [see (3)]. To eliminate edge effects in the shape of the receiver bandwidth, we used only the central 12-MHz of the 16-MHz spectrum. Thus, the time resolution from the delay was $0.04167 \mu\text{s}$, rather than the original $0.03125 \mu\text{s}$. The shape of the compact component should correspond to the function $\text{sinc}(\pi\Delta\nu\tau) = \sin(\pi\Delta\nu\tau)/(\pi\Delta\nu\tau)$, where $\Delta\nu$ is the analysis bandwidth (12 MHz). This function is zero when $\tau = 2 \times 0.04167 = 0.0833 \mu\text{s}$. For our purposes, it is convenient to represent a section of the sinc function with a parabolic curve in the form $y(x) = a(1 - kx^2)$ with the coefficient $k = 145$, for which y vanishes when $x = 0.0833 \mu\text{s}$. This approximation yields for the area beneath the central peak

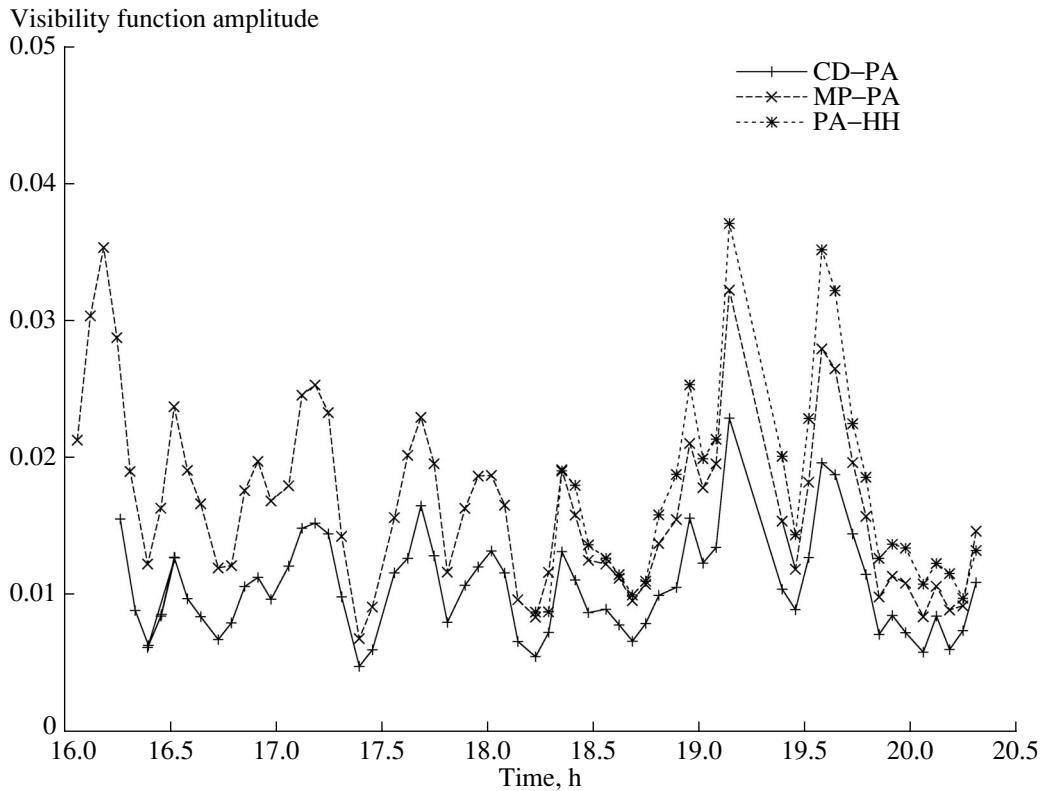


Fig. 5. Observations of B1749–28 on May 26, 2014 showing scintillation of the visibility amplitudes for three baselines between ground radio telescopes: Ceduna–Parkes (CD–PA), Mopra–Parkes (MP–PA), and Parkes–Hartebeesthoek (PA–HH). The amplitude scale is uncalibrated (i.e., the amplitudes are given in units of the correlation coefficient).

$S = (4/3)adt$, where a is the amplitude of the central peak and dt is its half-width ($dt = 0.0833 \mu\text{s}$). The resulting relative visibility amplitudes are presented in Fig. 2b as a function of the projected baseline averaged over 20-minute scans. The half-width of the extended feature approximated using a Lorentz function is contained in the interval 270–350 ns.

The substructure of the scattering disk is manifest through an analysis of sections of the two-dimensional cross-correlation between the interferometer responses (spots in the delay–fringe frequency diagram) obtained for the channels receiving left and right circular polarization. Examples of such sections in delay are shown in Figs. 6c and 6d for the (d) Parkes–Hartebeesthoek and RadioAstron–Parkes (c) baselines. Three components were identified in the structure of the spot: a compact Gaussian feature with a half-width $1/\Delta\nu$, a more extended Gaussian with a characteristic half-width of 270–320 ns (which corresponds to the width of the Lorentzian feature in the spot), and an exponential component whose amplitude falls by a factor of e over 500–600 ns. The amplitudes of the compact and medium Gaussian components are roughly equal, while the amplitude of the exponential component is a factor of two to three lower.

The behavior of the visibility amplitude as a function of the projected baseline is shown in Fig. 2b. The decrease in the amplitude on the longest ground–ground baselines and the complete absence of a central peak in the visibility function on ground–space baselines, in principle, enables measurement of the diameter of the scattering disk (θ_H) using (4), as was done for the pulsar B1641–45. The solid curve in Fig. 2b shows the resulting solution, which corresponds to $\theta_H = 0.5 \pm 0.2 \text{ mas}$ with $\alpha = 4$. The resulting value for the scattering angle is determined with a relatively low accuracy of about 30%, because no measurements on intermediate projected baselines near 20 000 km were available. As a result, an approximate estimate of the distance from the observer to the screen was obtained; the admissible position of the screen lies in the interval from 0.6 to 0.8 of the total distance from the observer to the pulsar, which we take to be 1.3 kpc.

The observed strong scintillation of the radio intensity of the pulsar, manifest as variations in the visibility amplitude (Fig. 5), enables measurement of the observed drift velocity of the diffraction pattern. For this, we compared the scintillation curves obtained from the auto-correlation spectra for the most widely separated radio telescopes, ATCA (AT) and

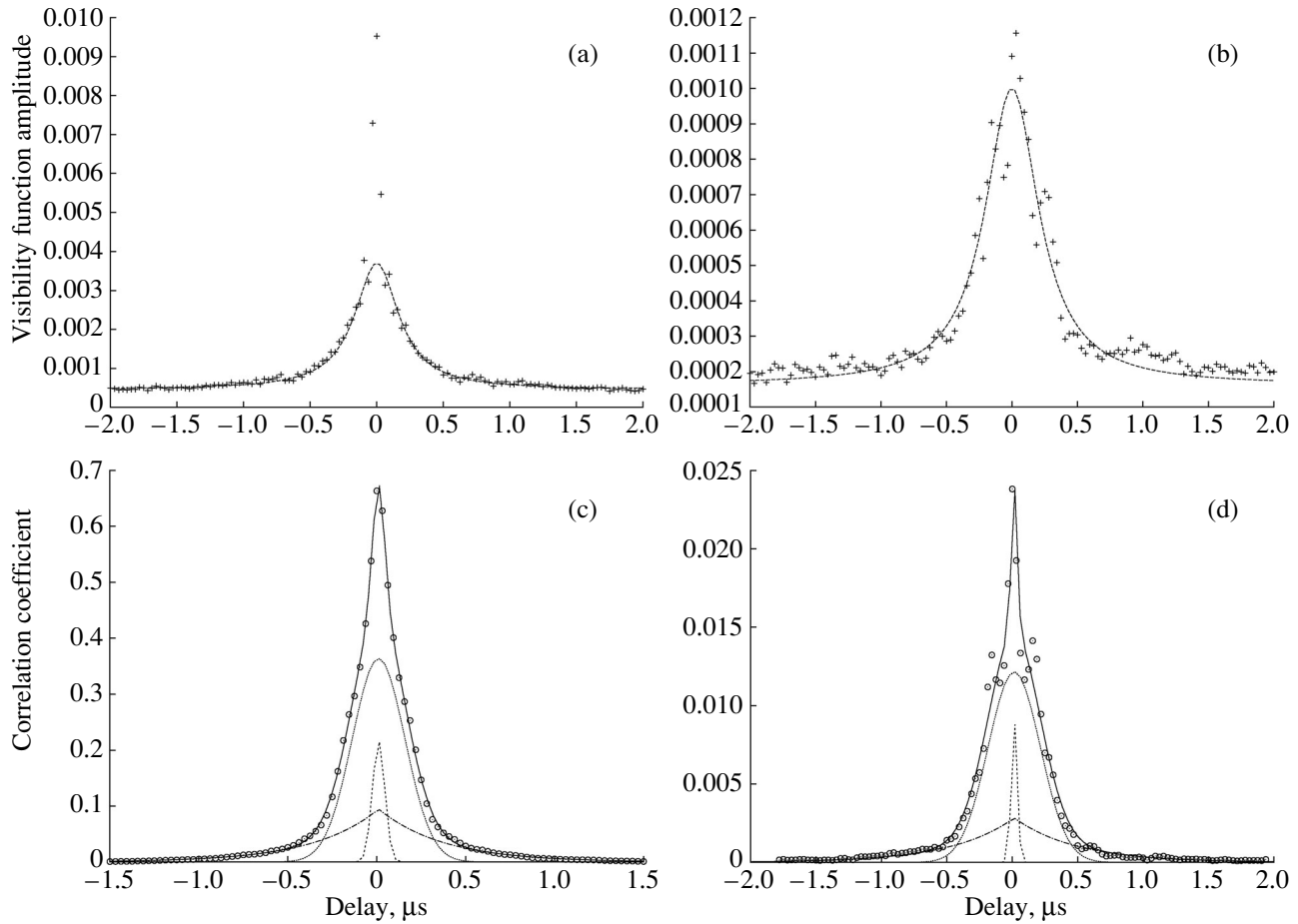


Fig. 6. The pulsar B1749–28. Panels (a) and (b) show a delay cross section on the delay–fringe frequency diagram for (a) the Ceduna–Parkes ground–ground baseline (a central peak is observed) and (b) the RadioAstron–Parkes space–ground baseline (there is no central peak). The interferometer response was first determined over 225-s intervals, after which five diagrams over a single observing scan (20 min) were averaged. The amplitude has not been calibrated to take into account the signal-to-noise ratio (SNR). The dashed curves show fits to the data using a Lorentzian function. Panels (c) and (d) show a delay cross section on the two-dimensional correlation function between the interferometer responses obtained for receiver channels with left and right circular polarization for (c) the 9000-km Parkes–Hartebeesthoek baseline and (d) the 120 000-km RadioAstron–Parkes baseline. The solid curve shows the sum of fits to three component functions represented by the dotted, dashed, and dot-dashed curves.

Hartebeesthoek (HH) and Parkes (PA) and Hartebeesthoek (HH). An example of a cross-correlation function (CCF) between the scintillation curves for the telescopes AT and HH obtained in the channel receiving left circular polarization in the upper sideband is presented in Fig. 7 (for a selected scintillation spot; such spots are clearly visible in the dynamic spectrum in Fig. 4). The position of the CCF maximum was determined by fitting a Gaussian to a section of the CCF near its peak. An appreciable shift of the CCF maximum for the correlation between the Australian telescopes (ATCA, Parkes) and between Australia and South Africa (Hartebeesthoek) is observed. Values for the delay of the scintillation pattern between 60 and 90 s were obtained for various combinations of telescopes, polarization channels, sub-bands, and

scintillation spots. This corresponds to drift velocities for the diffraction pattern V_{obs} from 110 to 160 km/s. The proper motion of the pulsar B1749–28 measured by Fomalont et al. [25] corresponds to $V_{\text{T}} = 40 \pm 30$ km/s for our adopted distance to the pulsar of 1.3 kpc.

To obtain the observed drift velocity of the diffraction pattern in a model with a thin scattering screen, this screen must be located fairly close to the pulsar:

$$V_{\text{obs}} = V_{\text{T}} \frac{d}{D - d}, \quad (6)$$

where d is the distance from the observer to the scattering screen.

For the mean values of the velocities V_{T} and V_{obs} , this yields $d/D = 0.78$, in satisfactory agreement

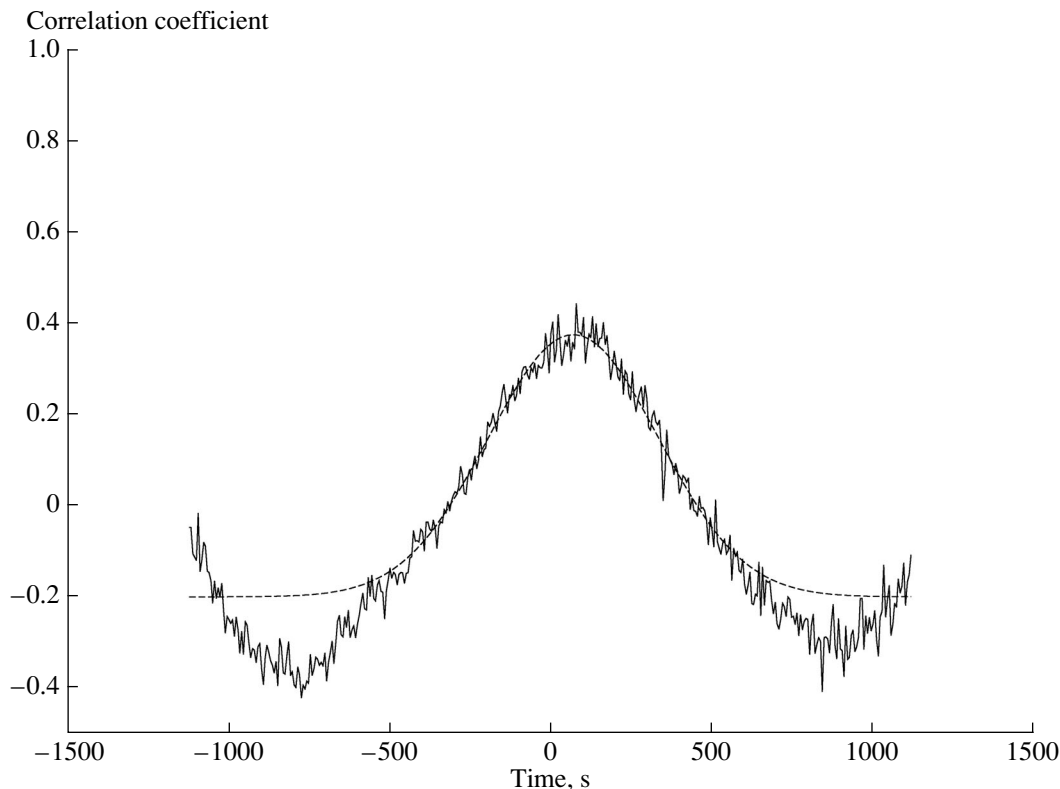


Fig. 7. The pulsar B1749–28. An example of the cross correlation between the scintillation curves for the telescope pair AT and HH for a selected scintillation spot. The shift in the maximum is 70 s, which corresponds to a drift velocity for the diffraction pattern of 130 km/s.

with our derived distance from the observer to the screen, estimated above using relation (5) between the scattering angle and the scattering time scale. In fact, the distance to B1729–28 is known only with large uncertainty [18], $d \sim 0.1\text{--}1.3$ kpc. Accordingly, the estimate of the distance to the scattering screen is also uncertain. In our view, a distant location for the pulsar (≈ 1.3 kpc) is preferable, in which case it coincides with the Sagittarius–Carina spiral arm, and several objects that can potentially be identified with the scattering screen are located along the line of sight. These objects include the H II (ionized-hydrogen) region RCW 142 (G0.55–0.85) and an OH/IR region [26, 27], which is accompanied by an extended envelope, which could serve as the scattering screen. If we adopt the mean ratio d/D of the estimates obtained using (5) and (6), 0.73 ± 0.1 , the distance to the scattering screen is 0.95 kpc for $D = 1.3$ kpc.

6. THE PULSAR B1933+16

The pulsar B1933+16 was observed simultaneously at two frequencies over 1.5 hours on August 1, 2013. In connection with the characteristics of the

SRT operation (see Section 2), the 316-MHz observations were carried out in right circular polarization in the upper sub-band, while the 1668-MHz observations were carried out in left circular polarization in both sub-bands. The 92-cm observations were conducted with the participation of the Westerbork Synthesis Radio Telescope (WSRT) and the 25-m St. Croix VLBA antenna; the 18-cm observations involved the participation of the 300-m Arecibo radio telescope and two 32-m radio telescopes, in Torun and Svetloe. It was not possible to obtain useful data from the St. Croix antenna due to incorrect setting of the gain of the receiver system. Jump-like variations in the dispersion of the signal were observed in the Torun data, which likewise hindered their use in our reduction.

The conditions for the observations were chosen such that the ground–space baseline progressively increased with time, from 1150 to 23 000 km at 316 MHz (from 1.2 to 25 million wavelengths, $M\lambda$) and from 6400 to 28 000 km at 1668 MHz (from 41 to 160 $M\lambda$). At both frequencies, the visibility amplitude remain roughly constant during the averaging of any number of cross-correlation spectra within a single scan of duration 9.5 min. Therefore, this amplitude was determined over an interval equal

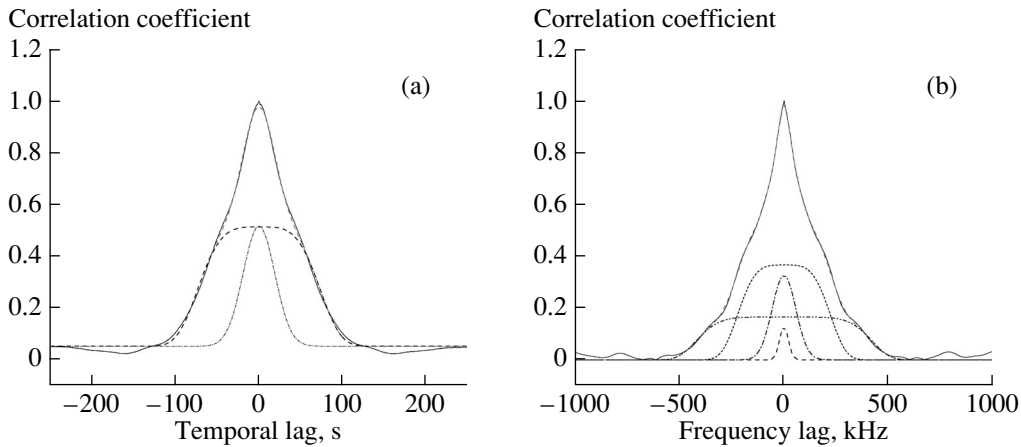


Fig. 8. The pulsar B1933+16. (a) Time and (b) frequency cross sections of the two-dimensional cross-correlation between the dynamic spectra in the two polarizations at 1668 MHz obtained at the Arecibo telescope. The solid curves show complex approximating functions, and the various discontinuous curves their components.

to a full scan. Due to the insufficient sensitivity of the SRT, the calibration of all amplitudes was conducted using (2). The visibility amplitude on the WSRT–RadioAstron baseline (316 MHz) decreased smoothly from its value on the minimum baselines out to baselines of $11 M\lambda$. Figure 2c shows the dependence of the visibility amplitude on the projected baseline at 316 MHz, and Fig. 2d the same for 1668 MHz. The solid curves present the results of fitting using formula (4). There is no central peak on long baselines. A decrease in the visibility amplitude in both sub-bands is observed on the Arecibo–RadioAstron baseline (1668 MHz), right to the longest baselines. These data are in good agreement with the amplitudes obtained on the shorter Arecibo–Svetloe baseline. The amplitudes obtained on the RadioAstron–Svetloe baseline have a high dispersion and lower mean, due to the low sensitivities of both telescopes. This baseline was not included in our subsequent analysis. Since we obtained a good distribution of points with increasing projected baselines for this pulsar, we left the index α as a free parameter in our fitting. Fitting using (4) with the free parameter α yielded for the second of three realizations, presented in Figs. 2c, 2d, the value $\alpha = 3.7 \pm 0.4$. However, we used the index $\alpha = 4$ in our final fitting everywhere in this study. The diameter of the scattering disk was found to be $\theta_H = 12.3 \pm 0.6$ mas at 316 MHz, in good agreement with earlier measurements (15.2 ± 1.3 mas [4]), and $\theta_H = 0.84 \pm 0.04$ mas at 1668 MHz.

The values $\Delta\nu_d = 110$ kHz and $\Delta t_{sc} = 45$ s were measured at 1670 MHz in [28]. Of the various telescopes used, only Arecibo has sufficiently high sensitivity to enable analysis of the scintillation pattern in the dynamic spectra. Therefore, we determined $\Delta\nu_d$ and Δt_{sc} only from the dynamic auto-correlation

spectra obtained for this radio telescope. The shapes of frequency and time cross sections of the CCF between the dynamic spectra obtained in the left and right circular polarization channels display a complex, multi-component structure.

The time cross section can be fit well using the sum of a Gaussian and a function of the form $\exp(-x^4)$ (Fig. 8a). The FWHM of the narrow Gaussian component is 41.6 ± 0.5 s, while the FWHM of the broader base is 134 ± 2 s. The frequency cross section must be fitted using three, and sometimes four, functions, each of which describes a certain frequency scale (see Fig. 8b). We used a sum of two Gaussians and a function of the form $\exp(-x^4)$ for the fitting. This yielded for the three FWHM values 50.4 ± 1.1 kHz, 144 ± 3 kHz, and 444 ± 2 kHz. We suggest that the more compact features correspond to the scintillation time scale and the decorrelation bandwidth, while the more extended component is the result of their superposition. In this case, the scattering time scale is $\tau_{sc} = 3.2 \pm 0.1 \mu\text{s}$.

The distance to this pulsar is not known well. An admissible range of distances of 2.9–5.0 kpc is given in [18]. If the plasma were distributed uniformly, the scattering angle given by the formula $\theta_H^2 = 16 \ln 2(c\tau_{sc}/D)$ would be about 2 mas for the mean distance of 3.7 kpc, which is a twice the measured value. The distance to the screen in a model with a thin scattering screen is 2.7 ± 0.1 kpc, or $0.7D$, for the adopted distance to the pulsar of 3.7 kpc.

Figure 9 shows the secondary spectrum at 1668 MHz obtained by means of a two-dimensional Fourier transform of the dynamic spectrum. In addition to the large central spot, we can note other individual structures extending along parabolic arcs

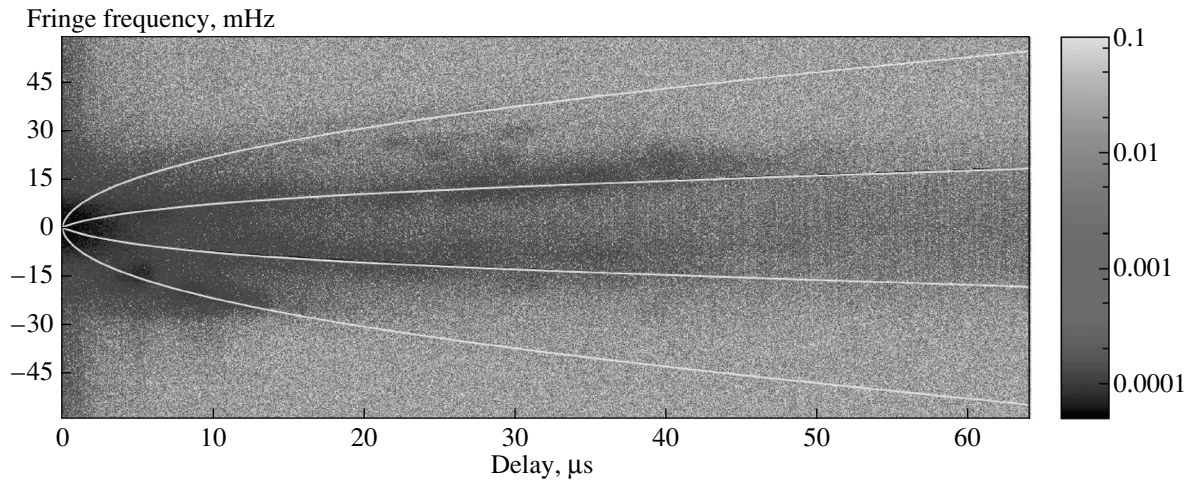


Fig. 9. The pulsar B1933+16. Secondary dynamic auto-correlation spectrum obtained on the Arecibo telescope at 1668 MHz. The curves show fits to the spectrum using parabolic arcs. The inner parabola corresponds to a screen located at a distance of 3.1 kpc from the Earth, and the outer to a screen located 1.3 kpc from the Earth.

with their vertices at the center of the secondary spectrum. Such arcs were first detected and studied in [6, 29, 30]. The position of one or more (according to the number of arcs) scattering screens can be determined independently from the previous estimates based on the shapes of these parabolas, as was proposed in [30]. The dependence between the delay f_ν and the fringe frequency f_t can be specified in the form $f_\nu = af_t^2$, where the coefficient a is equal to

$$a = \frac{Ds(1-s)}{2c} \left(\frac{\lambda}{V_\perp} \right)^2, \quad (7)$$

where s is the distance from the pulsar to the screen in units of D , s can be expressed $s = 1 - d/D$, λ is the observing wavelength, and $V_\perp = (1-s)V_{p\perp} + sV_{obs\perp} - V_{screen\perp}$, where $V_{p\perp}$, $V_{obs\perp}$, and $V_{screen\perp}$ are the tangential velocities of the pulsar, observer, and screen, respectively.

The proper motion of the pulsar is 13 mas/year [31], which gives a velocity of 220 km/s at a distance of 3.7 kpc. We assumed that the speeds of the Earth and the screen were appreciably lower than that of the pulsar. We determined the value of d for the two arcs indicated in Fig. 9, obtaining $d = 0.84D$ for the inner arc and $d = 0.35D$ for the outer arc. This yields distances from the observer to the screens of 3.1 and 1.3 kpc.

As for B1641–45, we analyzed the auto-correlation spectra at 316 MHz for the WSRT with high resolution by reducing the data using the method of pre-detection dispersion compensation with a frequency resolution of 50 Hz ($N_{ch} = 320\,000$). We constructed the CCF for the mean spectra obtained in the channels receiving left and right circular polarization, for

signals in and outside the pulse window. In spite of the substantial unresolved feature at zero frequency shift, it was possible to distinguish structure that was present in spectra inside the pulse window but absent from the spectra outside this window. Fitting this feature with an exponential function $C(d\nu) = a + b \cdot \exp(-c|d\nu|)$ yielded $C = 0.0026 \pm 0.0013$, which corresponds to a decorrelation bandwidth of 250 ± 150 Hz. This, in turn, yields for the scattering time scale $\tau_{sc} = 0.6 \pm 0.4$ ms. The distance from the observer to the scattering screen determined using (5) is then a factor of 0.7 times the total distance to the pulsar, or 2.6 kpc. Given the uncertainty in the estimate of τ_{sc} , the screen could be located at distances from 1.7 to 3 kpc, for the adopted distance to the pulsar of 3.7 kpc. Since we have independent measurements of τ_{sc} at two frequencies, we can again estimate the power-law index α to be $\alpha = (3.8 - 5.2)$, in good agreement with our previous estimate obtained from the scattering angle.

7. CONCLUSION

We have used the RadioAstron ground–space interferometer and a number of ground–ground baselines to investigate the distribution of interstellar plasma in the directions of the three distant pulsars B1641–45, B1749–28, and B1933+16, which are located near the plane of the Milky Way, subjecting their radio emission to strong scattering. The dependence of the calibrated visibility amplitudes as a function of projected baseline was used to measure the scattering angles for all three pulsars. We also measured the time scale for scatter broadening of the pulses due to inhomogeneities in the interstellar

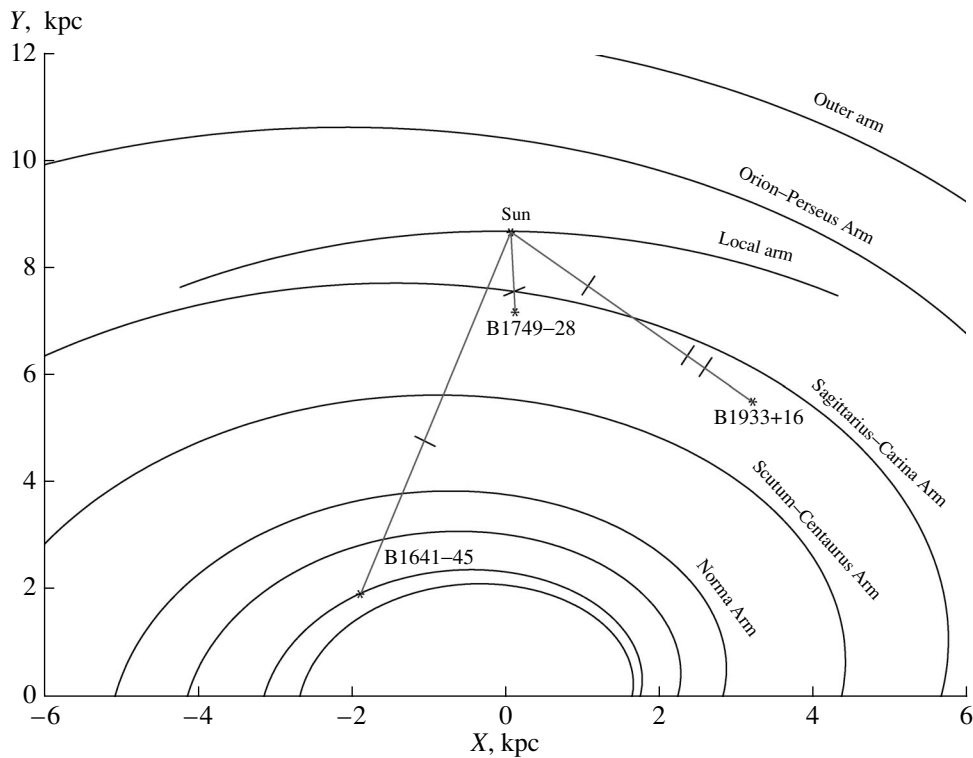


Fig. 10. Locations of the pulsars relative to spiral arms of the Galaxy. The asterisks mark the positions of the Sun and the pulsars B1641–45, B1933+16, and B1749–28. The solid dark curves denote spiral arms of the Galaxy. The ticks along the lines of sight indicate the positions of scattering screens we have derived based on our estimates.

plasma from the dependence of the visibility amplitude $V(\tau)$ on the delay or the shape of the tail of the mean pulse profile. Comparison of the scattering angle and scatter-broadening time scale in a model with a thin screen enabled localization of the thin screens along the lines of sight from the observer to the pulsars.

Figure 10 compares our results with the spiral arm structure of the Galaxy, according to the data of [32]. A model with four spiral arms was used here. The inferred effective scattering screens are located near Galactic spiral arms, where the appearance of appreciable inhomogeneities in the electron density of the interstellar plasma is most likely. Our adopted distances to the pulsars are presented in the second-last column in Table 2, while the derived positions of the effective screens are given in the last column of Table 2 and marked by ticks along the pulsar lines of sight in Fig. 10. Note that a model with scattering plasma uniformly distributed along the line of sight is not suitable for any of the pulsars. The inferred scattering screens are identified with real objects located along the lines of sight toward these pulsars G339.1–04 (PSR B1641–45) and G0.55–0.85 (PSR B1749–28).

For B1933+16, we also estimated the distance of the screen at two frequencies using relation (5),

which yielded similar values of 2.7 kpc at 1668 MHz and 2.6 kpc at 316 MHz for the adopted distance to the pulsar $D = 3.7$ kpc. In addition, the curvature of parabolic arcs at 1668 MHz was used to infer the presence of two screens at distances of 1.3 and 3.1 kpc, the latter of which agrees with the distance determined from the scattering angle. We conclude that our investigation of the structure of the interstellar plasma based on the analysis of VLBI observations of pulsars using the RadioAstron ground-space interferometer has enabled the identification of specific layers that are responsible for the main contribution to the observed scattering of the radiation of these pulsars, with these layers located near spiral arms of the Galaxy.

ACKNOWLEDGMENTS

RadioAstron is a project of the Astro Space Center of the P.N. Lebedev Institute of the Russian Academy of Sciences and the S.A. Lavochkin Research Industrial Association, under contract to the Russian Space Agency, together with many science and technological organizations in Russia and other countries.

The results presented here are partially based on observations carried out on radio telescopes of the In-

stitute of Applied Astronomy of the Russian Academy of Sciences.

The studies presented here are partially based on the results of observations with the European VLBI Network, as well as observations on the Arecibo telescope, telescopes of the National Radio Astronomy Organization (NRAO, USA), and telescopes of the Australian Telescope National Facility (ATNF, Australia and the University of Tasmania).

This work was supported by the Russian Foundation for Basic Research (13-02-00460) and the program of the Presidium of the Russian Academy of Sciences “Transitional and Explosive Processes in Astrophysics.”

REFERENCES

1. P. A. G. Scheuer, *Nature* **218**, 920 (1968).
2. B. J. Rickett, *Ann. Rev. Astron. Astrophys.* **15**, 479 (1977).
3. B. J. Rickett, *Ann. Rev. Astron. Astrophys.* **28**, 561 (1990).
4. C. R. Gwinn, N. Bartel, and J. M. Cordes, *Astrophys. J.* **410**, 673 (1993).
5. C. R. Gwinn, M. C. Britton, J. E. Reynolds, D. L. Jauncey, E. A. King, P. M. McCulloch, J. E. J. Lovell, and R. A. Preston, *Astrophys. J.* **505**, 928 (1998).
6. D. R. Stinebring, M. A. McLaughlin, J. M. Cordes, K. M. Becker, J. E. Espinoza Goodman, M. A. Kramer, J. L. Sheppard, and C. T. Smith, *Astrophys. J.* **549**, 97 (2001).
7. K. M. Desai, C. R. Gwinn, J. Reynolds, E. A. King, D. Jauncey, C. Flanagan, G. Nicolson, R. A. Preston, and D. L. Jones, *Astrophys. J.* **393**, L75 (1992).
8. N. Bartel, M. I. Ratner, I. I. Shapiro, R. J. Cappallo, A. E. E. Rodgers, and A. R. Whitney, *Astron. J.* **90**, 2532 (1985).
9. M. V. Popov, A. S. Andrianov, N. Bartel, C. R. Gwinn, M. D. Johnson, B. C. Joshi, N. S. Kardashev, R. Karuppusamy, Y. Y. Kovalev, M. Kramer, A. G. Rudnitskii, E. R. Safutdinov, V. I. Shishov, T. V. Smirnova, V. A. Soglasnov, J. A. Zensus, and V. I. Zhuravlev, *Astrophys. J.* **822**, 96 (2016).
10. A. G. Rudnitskii, R. Karuppusami, M. V. Popov, and V. A. Soglasnov, *Astron. Rep.* **60**, 211 (2016).
11. T. V. Smirnova, V. I. Shishov, M. V. Popov, C. R. Gwinn, J. M. Anderson, A. S. Andrianov, N. Bartel, A. Deller, M. D. Johnson, B. C. Joshi, N. S. Kardashev, R. Karuppusamy, Y. Y. Kovalev, M. Kramer, V. A. Soglasnov, J. A. Zensus, and V. I. Zhuravlev, *Astrophys. J.* **786**, 115 (2014).
12. N. S. Kardashev, V. V. Khartov, V. V. Abramov, V. Yu. Avdeev, A. V. Alakoz, Yu. A. Aleksandrov, S. Ananthakrishnan, V. V. Andreyanov, A. S. Andrianov, N. M. Antonov, M. I. Artyukhov, M. Yu. Arkhipov, W. Baan, N. G. Babakin, V. E. Babushkin, et al., *Astron. Rep.* **57**, 153 (2013).
13. A. S. Andrianov, I. A. Girin, V. E. Zharov, V. I. Kostenko, S. F. Likhachev, and M. V. Shatskaya, *Vestn. NPO Lavochkina* **24** (3), 55 (2014).
14. R. N. Manchester, G. B. Hobbs, A. Teoh, and M. Hobbs, *Astrophys. J.* **129**, 1993 (2005).
15. W. Pence, *ASP Conf. Ser.* **172**, 487 (1999).
16. J. Goodman and R. Narayan, *Mon. Not. R. Astron. Soc.* **238**, 963 (1989).
17. C. R. Gwinn, *Astrophys. J.* **554**, 1197 (2001).
18. J. P. W. Verbiest, J. M. Weisberg, A. A. Chael, K. J. Lee, and D. R. Lorimer, *Astrophys. J.* **755**, 39 (2012).
19. T. H. Hankins, *Astrophys. J.* **169**, 487 (1971).
20. T. H. Hankins and B. J. Rickett, *Methods Comput. Phys.* **14**, 55 (1975).
21. C. R. Gwinn, N. Bartel, J. M. Cordes, A. Wolszczan, and R. L. Mutel, *Astrophys. J.* **334**, L13 (1988).
22. S. F. Likhachev, *Doctoral (Phys. Math.) Dissertation* (2007). <http://fizmathim.com/sintez-i-analiz-izobrazheniy-metodami-nazemnoy-i-kosmicheskoy-radiointerferometrii#ixzz46MTrNGCb>.
23. M. C. Britton, C. R. Gwinn, and M. J. Ojeda, *Astrophys. J.* **501**, L101 (1998).
24. J. M. Weisberg, S. Johnston, B. Koribalski, and S. Stanimirovic, *Science* **309**, 106 (2005).
25. E. B. Fomalont, W. M. Goss, R. W. Manchester, and A. G. Lyne, *Mon. Not. R. Astron. Soc.* **286**, 81 (1997).
26. F. F. Gardner and J. B. Whiteoak, *Mon. Not. R. Astron. Soc.* **171**, 29 (1975).
27. J. R. D. Lepine, R. Ortiz, and N. Epchtein, *Astron. Astrophys.* **299**, 453 (1995).
28. J. A. Roberts and J. G. Ables, *Mon. Not. R. Astron. Soc.* **201**, 1119 (1982).
29. A. S. Hill, D. R. Stinebring, and H. A. Webber, *Astrophys. J.* **599**, 457 (2003).
30. J. M. Cordes, B. J. Rickett, D. R. Stinebring, and W. A. Coles, *Astrophys. J.* **637**, 346 (2006).
31. G. Hobbs, D. R. Lorimer, A. G. Lyne, and M. Kramer, *Mon. Not. R. Astron. Soc.* **360**, 974 (2005).
32. L. G. Hou and J. L. Han, *Astron. Astrophys.* **569**, id. A125 (2014).

Translated by D. Gabuzda